IJECBE (2025), **3**, **1**, 91–116
Received (5 March 2025) / Revised (19 April 2025)
Accepted (21 January 2025) / Published (30 May 2025)
https://doi.org/10.62146/ijecbe.v3i1.108
https://ijecbe.ui.ac.id
ISSN 3026-5258

IJECBE

International Journal of Electrical, Computer and Biomedical Engineering

RESEARCH ARTICLE

Day-Ahead Solar Power Forecasting Using a Hybrid Model Combining Regression and Physical Model Chain

Erwin Pauang Pongmasakke,[*†‡¶] Jian-Hong Liu,[‡] and Budi Sudiarto[†]

†Department of Electrical Engineering, Faculty of Engineering, Universitas Indonesia, Depok, Indonesia
‡Department of Electrical Engineering, National Taiwan University of Science and Technology, Taipei, Republic of China (Taiwan)
¶PT. Perusahaan Listrik Negara, PLN (Persero)
*Corresponding author. Email: erwin.pauang@pln.co.id

Abstract

Solar power forecasting is essential for integrating PV plants into power grids, ensuring stability and aiding system operators (SOs) in decision-making. However, existing day-ahead models struggle with rapid weather changes, while deep learning models require extensive historical data, making them impractical for new PV plants. This study proposes a hybrid approach combining the XGBoost algorithm for hourly solar irradiance prediction using Numerical Weather Prediction (NWP) data and a physical model to convert irradiance into power. The XGBoost model is periodically retrained via a sliding window mechanism to adapt to dynamic weather conditions. A case study using two years of 271 kWp PV data from NIST (US) and historical NWP data from ECMWF ENS for GHI forecasting, alongside ECMWF HRES for power conversion, demonstrated the method's effectiveness. Using just one week of historical data for initial training, the model achieved an nRMSE of 13.35%–13.53%, nMAE of 6.9%–7.03%, and nMBE of -2.03% to -0.29%. The proposed approach improves PV forecasting reliability for new plants with limited data, serving as an intermediary solution until sufficient historical data is available for deep learning models.

Keywords: Hybrid method, NWP, Physical model chain, Day-ahead PV power forecast, XGBoost

1. Introduction

The global transition toward sustainable energy systems is a pivotal response to the climate crisis, driven by the urgent need to reduce greenhouse gas emissions. Solar energy, being one of the most abundant and cleanest sources of power, plays a critical role in this vision. According to recent data, the price of solar PV systems has dropped by over 80% in the last ten years [1], making it one of the most affordable renewable energy options available. Innovations in materials, efficiency improvements, and integration with energy storage technologies have further enhanced the viability of solar energy as a reliable power source [2] and have driven the exponential growth of installed solar capacity worldwide [3].

Despite its advantages, solar power generation is inherently intermittent, as solar irradiance—the primary driver of PV power output—varies with weather conditions, time of day, and seasonal changes. This variability poses challenges for grid stability and reliability, making accurate forecasting essential.

A key factor influencing PV system output is Global Horizontal Irradiance (GHI), which represents the total solar radiation received per unit area on a horizontal surface, comprising both direct and diffuse sunlight. Direct Normal Irradiance (DNI) refers to sunlight traveling directly from the sun, while Diffuse Horizontal Irradiance (DHI) represents scattered sunlight reaching the Earth's surface from the atmosphere. Together, these components determine the amount of energy available for photovoltaic (PV) conversion.

Since solar irradiance fluctuates due to atmospheric conditions, Numerical Weather Prediction (NWP) data plays a crucial role in forecasting its variations [4]. NWP models simulate atmospheric processes using physical equations and observational data, generating forecasts for key meteorological variables such as cloud cover, temperature, humidity, wind speed, and pressure—all of which influence solar radiation. Beyond these weather parameters, NWP data also provide irradiance forecasts, making them a critical input for solar energy prediction.

Once solar irradiance reaches the PV system, its conversion into electricity depends on multiple physical factors, including PV cell material properties, the angle of incidence of sunlight, temperature, and environmental conditions. Additionally, system components such as inverters and panel configurations play a crucial role in overall performance. A model that considers all these factors is often referred to as a physical model chain [4].

As the share of solar power in the global energy mix continues to grow, the importance of robust forecasting models cannot be overstated. Short-term forecasting enables better decision-making in energy dispatch, balancing renewable generation with demand, and reducing reliance on fossil fuels. In particular, day-ahead forecasting plays a critical role in anticipating short-term fluctuations to help grid operators balance supply and demand, optimize energy storage, and maintain system stability.

Several studies such as [5], [6], [7], and [8] have examined the application of machine learning (ML) and artificial neural network (ANN) models for photovoltaic (PV) power forecasting. However, purely ML- or ANN-based models are highly dependent on extensive historical training data to generate accurate forecasts—a requirement that may not always be feasible in real-world applications.

Unlike physical models, ML-based methods do not incorporate predefined rules or domain knowledge, but instead learn patterns directly from data. Consequently, the availability of diverse and representative historical data becomes crucial for effective generalization. As highlighted by [8], achieving reliable accuracy with deep learning models often necessitates at least two years of historical data.

This research addresses the challenges of day-ahead forecasting resulting from the inherent intermittency of solar irradiance by using a hybrid approach that combines NWP data with a physical model chain and machine learning (ML) techniques. The motivation for this hybrid framework stems from the complementary strengths of both components: while physical models encapsulate the structured physics-based irradiation-to-power conversion, ML models excel at capturing complex, nonlinear relationships of irradiance forecast from NWP data. Furthermore, a sliding window mechanism is combined with the ML techniques to ensure model adaptability over time and maintain high forecast accuracy in dynamic environments.

By improving solar irradiance and solar power forecasting methods, this research contributes to the enhanced operational efficiency of PV systems, facilitates a better insight and decision-making for PV system operations and grid management. The remainder of this paper is organized as follows: **Section 2** Solar Irradiance and Irradiance-to-power Conversion, **Section 3** Methodology, **Section 4** Results and Discussion, and **Section 5** Conclusion and Future Work.

2. Solar Irradiance and Irradiance-to-power Conversion

2.1 Solar Irradiance

The solar irradiance received at the earth's surface is subject to several modifying factors, including atmospheric effects, seasonal variations, and diurnal patterns. Solar irradiance measured in [W/m^2] refers to the power per unit area received from the sun in the form of electromagnetic radiation. Generally, the relationship between DHI, DNI and GHI is shown as follows:

$$\begin{aligned} \mathrm{GHI} &= \mathrm{DNI} \cdot \cos(\theta_z) + \mathrm{DHI} \\ \mathrm{DHI} &= \mathrm{GHI} - \mathrm{DNI} \cdot \cos(\theta_z) \end{aligned} \tag{1}$$

Variables that directly related to solar irradiance are shown in the Table1.

Table 1. List of Variables and Their Symbols

Variable Name	Symbol
Solar Zenith Angle	θ_z
Angle of Incidence	θ_i
Panel Surface Tilt Angle	β
Panel Surface Azimuth Angle	γ
Solar Azimuth Angle	γ_s
Albedo	ρ

The relationship between those variables for the tilted surfaces can be mathematically expressed as:

$$\cos(\theta_i) = \cos(\theta_z)\cos(\beta) + \sin(\theta_z)\sin(\beta)\cos(\gamma - \gamma_s) \tag{2}$$

The European Centre for Medium-Range Weather Forecasts (ECMWF) provides two valuable real-time numerical weather prediction (NWP) datasets for global horizontal irradiance (GHI) forecasting: ECMWF ENS and ECMWF HRES. ECMWF ENS offers 15-day hourly ensemble forecasts, providing 50-ensemble members for GHI based on varying initial conditions, while ECMWF HRES delivers single prediction of 10-day hourly high-resolution atmospheric forecasts. Both datasets are issued four times daily at 00Z, 06Z, 12Z, and 18Z, with global coverage at $0.5^\circ \times 0.5^\circ$ and $0.1^\circ \times 0.1^\circ$ lon/lat spatial resolutions, respectively. This frequent release schedule, along with their comprehensive geographical coverage, makes them ideal for both day-ahead and intra-day solar forecasting, capturing atmospheric variability and improving the accuracy of solar irradiance predictions.

Although ECMWF data was historically restricted from public access, recent initiatives have significantly improved its availability. The first publicly accessible ECMWF ENS dataset was introduced in [9], while [10] facilitated broader access to ECMWF HRES for researchers and practitioners. In [7], ECMWF HRES data was employed to forecast day-ahead power production for the day-ahead market (DAM) in the Netherlands. Similarly, [11] utilized historical NWP forecasts from the Nordic MetCoOp system, which integrates HARMONIE-AROME models. Furthermore, [12] combined ECMWF NWP data with forecasts from the *European Organisation for the Exploitation of Meteorological Satellites* (EUMETSAT) to nowcast hourly PV energy production, demonstrating the versatility of NWP data in solar energy forecasting.

2.2 Irradiance-to-power Conversion

Irradiance-to-power conversion refers to the process that transforms incoming irradiance into produced power. While Long Short-Term Memory (LSTM) networks outperform models such as multiple linear regression, SARIMAX, and LASSO in day-ahead solar power forecasting given the input parameters [7], they require extensive historical data, which may not always be available, especially for new PV plants. Although these advanced techniques excel in capturing forecasting complexities, [8] suggests that at least three years of data are needed for deep learning to make reliable predictions, making them impractical for immediate forecasting needs such as for a newly-built PV plant. In contrast, physical model chains offer a solution as they do not require long historical data [13].

2.2.1 Physical Model Chain

The efficiency of irradiance-to-power conversion depends on PV cell materials, angle of incidence, temperature, and environmental conditions. A physical model chain, based on fundamental physics, simulates PV performance by incorporating solar irradiance, temperature, atmospheric conditions, and PV component characteristics like module efficiency and electrical behavior. A physical model it provides an interpretable, robust, and reliable framework for solar energy conversion.

Following a structured process from solar positioning to PV power output, a physical model chain sequentially links each step, forming a comprehensive, physics-based prediction of PV performance, as illustrated in Figure 1, adopted from [4]. This approach enables extrapolation beyond observed data, allowing simulations under extreme conditions. Unlike data-driven models, which may struggle outside their training range, physical models reliably predict PV behavior across diverse conditions.

Losses in the physical model chain include losses from surrounding obstructions, DC and AC cable losses due to resistance in the wiring, inverter losses during DC-to-AC conversion, and transformer losses from voltage adjustments. Some losses depend on site-specific factors such as device specifications (e.g., cable material, inverter efficiency) and site-specific conditions (e.g., shading profiles, soiling).

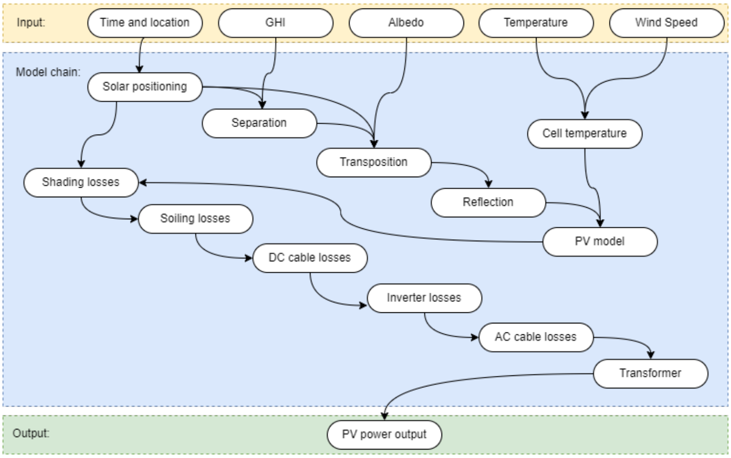

Figure 1. Physical model chain

2.3 *Forecasting Operationalization*

To fully leverage the advantages of day-ahead PV power forecasting, it must align seamlessly with the operational standards of real-world PV power system operators. [14] defines four key forecast parameters: forecast lead time ($\mathcal{L}$), which represents the time between the forecast submission and the first forecast; forecast resolution ($\mathcal{R}$), referring to the step size or time interval of the submitted forecasts; forecast horizon or span ($\mathcal{S}$), indicating the period between the first and last submitted forecasts; and forecast update rate ($\mathcal{U}$), which specifies how frequently forecasts are submitted.

Those parameters ensure that the forecast is both accurate and practical, mimicking the operational requirements of a real-world system operators such as HUPX in Hungary [5], CAISO in California [15], and China [16]. Figure 2 illustrates the forecast parameters.

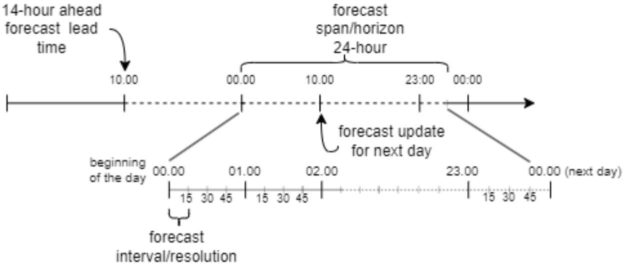

Figure 2. Forecast parameter

3. Methodology

3.1 *Hybrid Method*

Most solar power forecasting research focuses on either data-driven or physical models. To the best of the authors' knowledge, only two studies—[5] and [17]—have developed a two-step forecasting framework, where the first step involves GHI forecasting, followed by power forecasting in the second step.

This study presents a novel hybrid forecasting method that combines machine learning and physical modeling. The first stage employs `XGBoost` regression with a sliding window approach and periodic retraining mechanism, ensuring continuous adaptation to recent weather patterns without requiring extensive historical data. In the second stage, a physical model chain converts the predicted irradiance into AC power output, enhancing accuracy and practical applicability. This hybrid approach bridges the gap between data-driven and physics-based models, offering a robust and scalable solution for day-ahead PV power forecasting. Figure 3 illustrates the whole workflow.

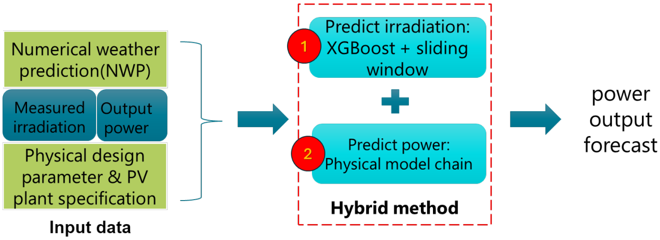

Figure 3. Research workflow

The forecast parameters used in this experiment – $\mathcal{L}^{24h}$, $\mathcal{R}^{15min}$, $\mathcal{S}^{24h}$, and $\mathcal{U}^{24h}$ – are aligned with real-world operational standards for day-ahead PV forecasting, as outlined in [5], [15], and [16].

3.1.1 *XGBoost Regression*

Extreme Gradient Boosting (`XGBoost`) is a supervised model commonly employed for solving multivariate regression and time series problems. `XGBoost` is a non-linear model, expected to capture temporal patterns and non-linear dynamics inherent in solar irradiance data.

`XGBoost` is an optimized gradient boosting algorithm that builds an ensemble of decision trees for predictive tasks. As an ensemble learning method, `XGBoost` combines multiple weak learners (typically decision trees) into a strong predictive model. Each new tree focuses on reducing the residual errors of previous ones, continuously improving performance. Figure 4 illustrates the `XGBoost` workflow [18].

The objective function $\mathcal{L}(\phi)$ of XGBoost is:

$$\mathcal{L}(\phi) = \sum_{i=1}^{n} l(y_i, \hat{y}_i) + \sum_{k=1}^{K} \omega(f_k) \tag{3}$$

where $l(y_i, \hat{y}_i)$ is the loss function that measures the difference between the true label (value) and the predicted label (value), y_i is the actual (observed) value or the true target, $\hat{y}_i = \sum_{k=1}^{K} f_k(x_i)$ is the predicted value, which is the sum of the output of the k-th tree for the input x_i, $\omega(f_k)$ is the regularization term, and K is the total number of trees.

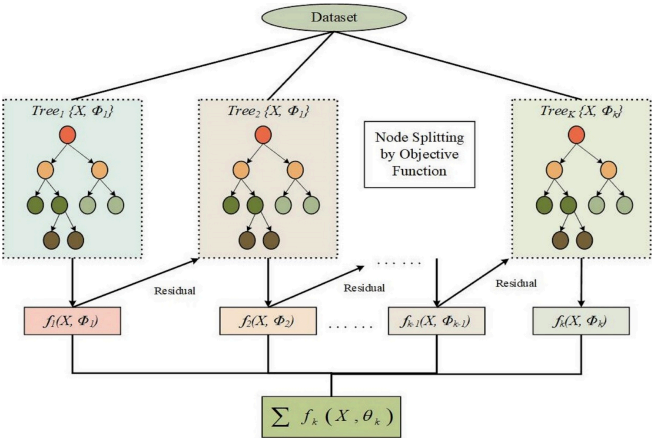

Figure 4. `XGBoost` flow

The `XGBoost` takes ECMWF ENS `ssrd` data (see Table 4) as the input features to produce GHI forecast. Hyperparameter tuning for the XGBoost model was performed using a grid search over the parameter ranges shown in Table 2. The number of boosting rounds was set to 100, with early stopping applied after 10 rounds without improvement on the validation set to prevent overfitting.

A sliding window approach with periodic retraining is employed for hourly irradiation prediction. This approach complements `XGBoost`, which does not require extensive historical data for effective learning. These mechanisms ensure that the model is continuously updated with the most recent data, effectively capturing the periodic and seasonal characteristics of solar irradiance. Figure 5 illustrates the integration of XGBoost with the sliding window and periodic retraining approach for hourly GHI prediction. The resulting hourly GHI forecast is then downscaled using cubic interpolation to achieve a 15-minute resolution, complying with $\mathcal{R}^{15min}$.

Table 2. Hyperparameter ranges used for XGBoost tuning

Hyperparameter	Values / Range
`max_depth`	{5, 8}
`learning_rate`	{0.05, 0.1}
`subsample`	{0.8, 1.0}
`min_child_weight`	{5, 8}
`gamma`	{0, 0.1}
`lambda`	0.1
`alpha`	{0.1, 0.2}
`colsample_bytree`	{0.8, 0.4}
`n_estimators`	100

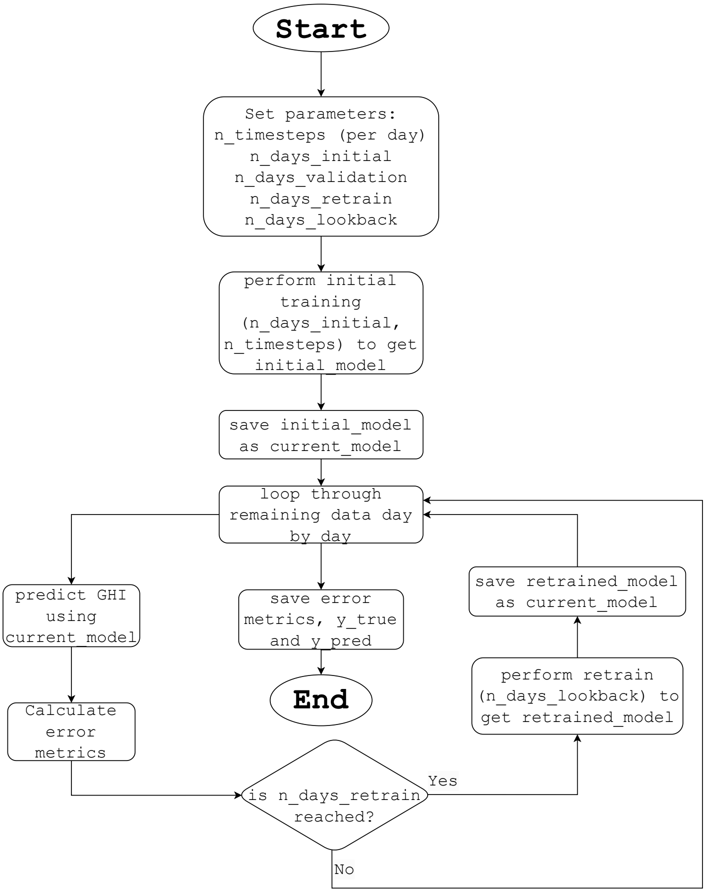

Figure 5. Flow of `XGBoost` with sliding window mechanism

3.1.2 Physical Model Chain

To calculate the output power given the predicted GHI from the XGBoost regression model, a set of physical models at each step is selected. The physical model chain requires additional input variables such as GHI forecast, solar zenith angle, solar azimuth angle, and extraterrestrial radiation constant. Table 3 summarizes the models used in each step of the physical model chain and details the model-specific variables.

Table 3. Physical Models and Required Inputs Variables

Physical Model	Reference	Input from ECMWF HRES
Separation (S)		
Erbs	[19]	dewpoint (`d2m`), pressure (`sp`)
DIRINT	[20]	dewpoint (`d2m`), pressure (`sp`)
Erbs-Driesse	[21]	dewpoint (`d2m`), pressure (`sp`)
Transposition		
Perez-Driesse	[21]	albedo (`fal`)
Reflection (R)		
ASHRAE	[22]	-
Physical	[23]	-
Martin-Ruiz	[24]	-
Cell temperature (C)		
SAPM	[25]	wind speed (`u10, v10`), ambient temperature (`t2m`)
PVSyst (Faiman)	[26]	wind speed (`u10, v10`), ambient temperature (`t2m`)
NOCT SAM	[27]	wind speed (`u10, v10`), ambient temperature (`t2m`)
PV Model (P)		
Evans	[28, 29]	-
De Soto (Single diode 6 param.)	[23]	-

Loss modeling is omitted, as it is highly system-specific. Instead, standard assumptions or average conditions are applied for practical implementations. Additionally, cubic spline interpolation is used to downscale temperature and wind speed forecasts from ECMWF HRES to comply with the $\mathcal{R}^{15min}$.

3.2 Dataset

The dataset used to test the proposed method consists mainly of ECMWF ENS and ECMWF HRES. As a reference, publicly accessible ground measurement GHI data from a well-maintained, research-grade sensor at the grid-connected solar PV arrays of the *National Institute of Standards and Technology* (NIST) [30] [31] is used to evaluate the proposed method. Missing values in the dataset are filled using weather station data from the same period, ensuring no gaps in ground truth GHI values. Figure 6 visualizes ground-measured GHI data between sunset and sunrise over two years. A summary of the dataset is provided in Table 4. Table 5 details the specifications of the NIST grid-connected ground PV array, while Figure 7 illustrates its location.

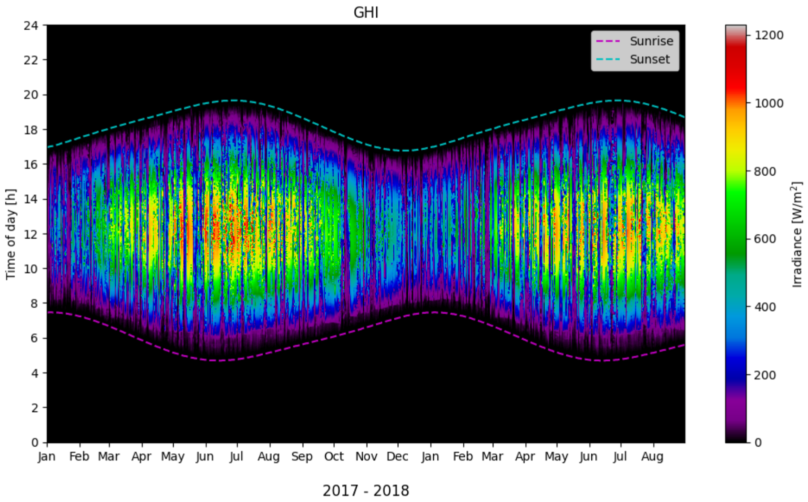

Figure 6. Heatmap of measured GHI

Table 4. Datasets and Variables

Item	Ground Truth (NIST)	ECMWF ENS	ECMWF HRES
Data period	1 Jan 2015–31 Dec 2018	1 Jan 2017–31 Dec 2018	1 Jan 2017–31 Dec 2020
Data resolution	1-min	1-hour	1-hour
Release time	-	00Z	00Z
Horizon	-	91 hours	91 hours
Variable			
Power output	`Power` [kW]	-	-
GHI	`GHI` [W/m^2]	`ssrd` [W/m^2]	-
DHI	`DHI` [W/m^2]	-	-
DNI	`DNI` [W/m^2]	-	-
Tilted irradiance	`POA irradiance` [W/m^2]	-	-
U wind component	-	-	`u10` [m/s]
V wind component	-	-	`v10` [m/s]
Surface pressure	-	-	`sp` [Pa]
Temperature	`Ambient temperature` [°C]	-	`t2m` [K]
Dewpoint	-	-	`d2m` [K]
Total column ozone	-	-	`tco3` [kg/m^2]
Forecast albedo	-	-	`fal`
Total column water vapor	-	-	`tcwv` [kg/m^2]

3.3 Evaluation and Metrics

The performance of the predicted results from both stages is evaluated using true values from the NIST dataset as references, as shown in Table 6. The cell temperature predictions from the cell temperature model cannot be directly validated due to the lack of relevant true measurements in the NIST dataset. Instead, the predicted cell temperature is compared to the measured module-backsheet temperature. The reflection loss model is unique as it does not have corresponding reference data in the NIST dataset. Consequently, its evaluation relies on the mean percentage of reflected irradiance, which provides an indirect measure of its performance.

Table 5. NIST Ground PV Array Specifications

Location	Gaithersburg, Maryland, US
Type	Ground-mounted, without tracker
Latitude [° N]	39.1319
Longitude [° E]	-77.2141
Elevation [m]	138
Panel Tilt [°]	5
Panel Azimuth [° from North]	180
Rated DC Power [kW]	271
Module Model	Sharp NU-U235F2
Module Technology	Monocrystalline silicon - front contact
Module Rated Power [W]	235
Number of Modules	1152
Module Per String	12
Numbner of Combiner Boxes	7
Number of Source Circuits (SC)	96
Inverter	PV Powered PVP260kW, 1 unit

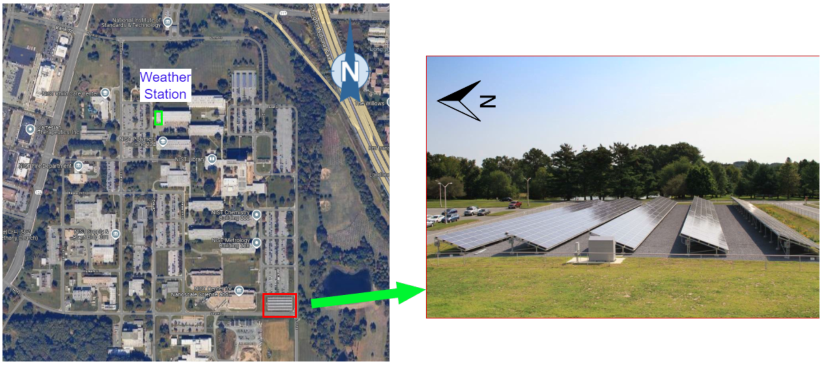

Figure 7. NIST ground PV array and weather station location

Table 6. Validation of Physical Model Chain Output

Model	Output Parameter	Validation Data Source
XGBoost Regression	Hourly GHI	Themopile Pyranometer
Separation	DNI dan DHI	Pyranometer Eppley 8-48 and Pyrheliometer Kipp & Zonen CHP 1
Transposition	POA	flat-plate Silicon IMT Solar Si-420TC.
PV Model	VDC, I, PDC	current, voltage and power from inverter PV Powered PVP260kW
Inverter	PAC	measured PAC by the inverter PV Powered PVP260kW
Cell temperature	cell temperature	Omega RTD-3-F3102-72-T

Three widely accepted metrics to evaluate the forecasting models' performance: root mean square error (RMSE) in Eq. 4, mean absolute error (MAE)in Eq. 5, and mean bias error (MBE) in Eq. 6. These metrics collectively provide a comprehensive analysis of the model's accuracy and bias, offer a balanced approach to analyze the trade-off between accuracy and interpretability in the model's predictive performance

$$\mathrm{RMSE} = \sqrt{\frac{1}{n}\sum_{i=1}^{n}\left(\hat{y}_i - y_i\right)^2} \tag{4}$$

$$\mathrm{MAE} = \frac{1}{n}\sum_{i=1}^{n}\left|\hat{y}_i - y_i\right| \tag{5}$$

$$\mathrm{MBE} = \frac{1}{n}\sum_{i=1}^{n}\left(\hat{y}_i - y_i\right) \tag{6}$$

4. Result and Discussion

4.1 GHI Forecast

Given the 50 ensemble-member predictors from the ECMWF ENS data and the true GHI values from the NIST dataset, several combinations of *n*-days initial training and *m*-days for periodic retraining were tested to predict hourly GHI using the XGBoost model. Combinations of 3, 7, 14, and 30 days for both *n*-days and *m*-days.

Table 7 presents the performance metrics for the overall predicted hourly GHI across all combinations of initial training and periodic retraining. The results indicate that the variation in RMSE is influenced by the choice of initial training duration and periodic retraining interval (sliding-window size). In general, for the same initial training duration, a periodic retraining interval of 3 days results in higher RMSE, MAE, and MBE values compared to periodic retraining intervals of 7, 14, and 30 days.

Regardless of the selection of initial training days, the RMSE for periodic retraining intervals of 7, 14, and 30 days ranges between 146.25 W/m^2 and 151.95 W/m^2. The MAE from roughly 91 W/m^2 to 94 W/m^2, and between –0.11 W/m^2 to 6.55 W/m^2 for MBE. Considering the small differences in RMSE, MAE, and MBE, the smallest initial training duration (e.g., 3, 7, or 14 days) is preferred as it requires only a small historical dataset. Table 8 compares the performance of the hourly irradiance forecast of the `XGBoost`, LSTM, and the persistence forecast for the given training days. For `XGBoost`, only the best result from the periodic retraining process is shown for each training day (based on the initial training period). The table confirms that the `XGBoost` forecast outperforms the persistence baseline forecast in terms of both RMSE and MAE. For all initial training days (3, 7, 14, and 30), the RMSE ranges from 146.25 to 148.34 W/m^2. Compared to LSTM, similar RMSE values are achieved when using 60, 90, 180, or 360 days of historical data to train the LSTM model.

Considering there is no significant difference in RMSE (as shown in Figure 8) and MAE (as shown in Figure 9) for initial training days of 3, 7, 14, and 30 for periodic retraining intervals of 7, 14, and 30 days, the combination of 3 or 7 initial training days with a periodic retraining interval of 7 or 14 days is preferred as the best model, as

Table 7. Performance Metrics Hourly GHI Forecast

Initial Training (Day)	Periodic Retraining (Day)	RMSE	MAE	MBE
3	3	166.12	105.04	-13.87
	7	151.49	93.86	**-0.11**
	14	147.39	91.89	-5.19
	30	**146.25**	**91.48**	-4.13
7	3	174.55	108.99	-20.59
	7	148.56	93.03	-3.78
	14	150.03	94.33	**-1.67**
	30	**147.57**	**91.44**	-5.22
14	3	170.29	106.88	-15.82
	7	**148.80**	93.43	**-3.32**
	14	149.61	93.29	-5.10
	30	149.37	**93.14**	-5.23
30	3	167.85	106.87	-13.56
	7	151.95	94.82	**-2.38**
	14	148.52	**93.76**	-6.55
	30	**148.34**	94.10	-4.47

Table 8. Performance of the Proposed Method for hourly GHI

Model	Training Days	RMSE	MAE	MBE
LSTM: Layer 1 (128 units, activation: tanh, dropout: 0.2) Layer 2 (128 units, activation: tanh, dropout: 0.2) Layer 3 (128 units, activation: ReLU, dropout: 0.2) Dense Layer	3	192.13	131.85	-60.28
	7	346.08	234.72	-193.88
	14	344.12	237.15	-181.43
	30	188.02	121.56	-71.05
	60	**140.62**	**87.61**	**-6.97**
	90	**140.15**	**89.55**	**-2.81**
	120	302.46	217.55	-110.58
	150	294.39	205.11	-125.54
	180	**132.33**	**84.52**	**3.76**
	360	**128.95**	**79.19**	**7.83**
XGBoost (proposed)	3	**146.25**	**91.48**	**-4.13**
	7	**147.57**	**91.44**	**-5.22**
	14	**148.80**	**93.43**	**-3.32**
	30	**148.34**	**94.10**	**-4.47**
Persistence	NA	**230.36**	**134.59**	**0.17**

it allows predictions to be made using limited historical data. Furthermore, Figure 10 demonstrates that predictions made with 7-day periodic retraining produce less bias compared to other periodic retraining options, regardless of the initial training days.

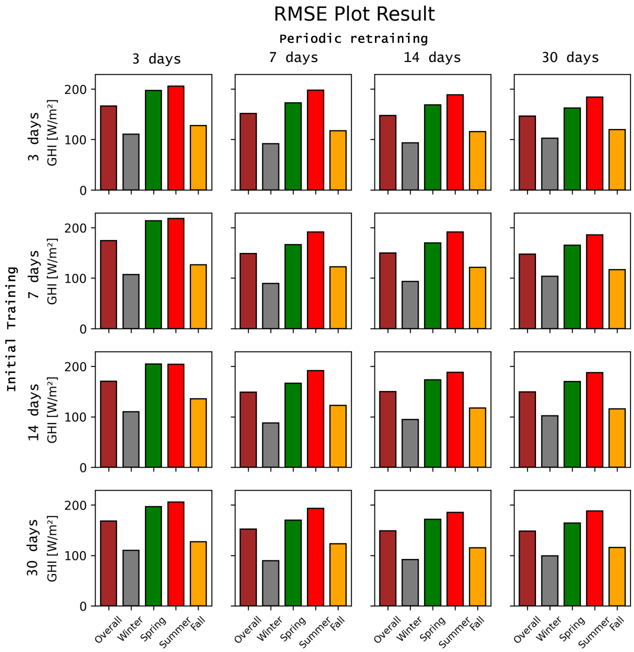

Figure 8. XGBoost RMSE performance

Figure 11 compares the actual GHI with the predicted GHI from the best-performing `XGBoost` model. To illustrate seasonal variations, a randomly sampled week from each season is plotted, highlighting the model's tendency to underestimate the true GHI, as reflected in the negative MBE values.

4.2 Physical Model Chain

4.2.1 Separation

Figure 12 presents the RMSE, MAE, and MBE metrics for DNI and DHI using the Erbs, DIRINT, and Erbs-Driesse separation models.

For DNI, DIRINT achieves the lowest RMSE (264.13 W/m^2), while Erbs-Driesse has the highest (295.45 W/m^2), with Erbs in between (278.31 W/m^2). MAE follows the same trend: 133.11, 141.06, and 149.89 W/m^2. However, for MBE, Erbs-Driesse performs best (–23.08 W/m^2), whereas DIRINT has nearly double the bias (–39.25 W/m^2). Overall, RMSE and MAE differences are minimal.

For DHI, Erbs-Driesse consistently outperforms Erbs and DIRINT across all metrics. The separation model's DNI and DHI outputs then proceed to the transposition stage in the physical model chain.

4.2.2 Transposition

Transposition model converts DNI and DHI from the separation model into POA irradiance at a given tilt . POA irradiance accounts for tilt, azimuth, and albedo.

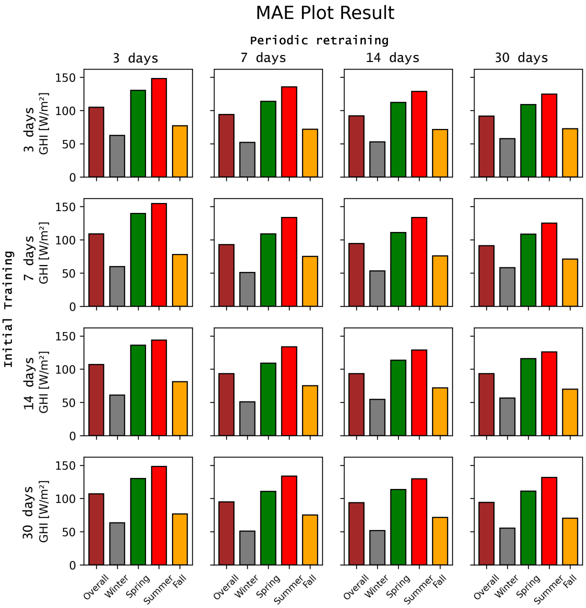

Figure 9. XGBoost MAE performance

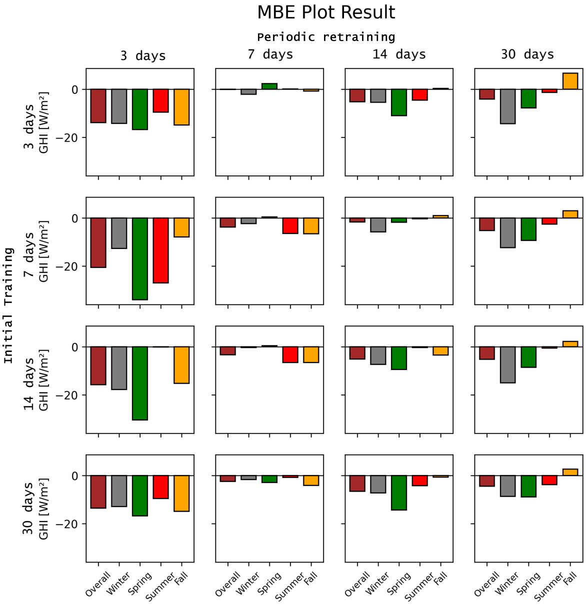

Figure 10. XGBoost MBE performance

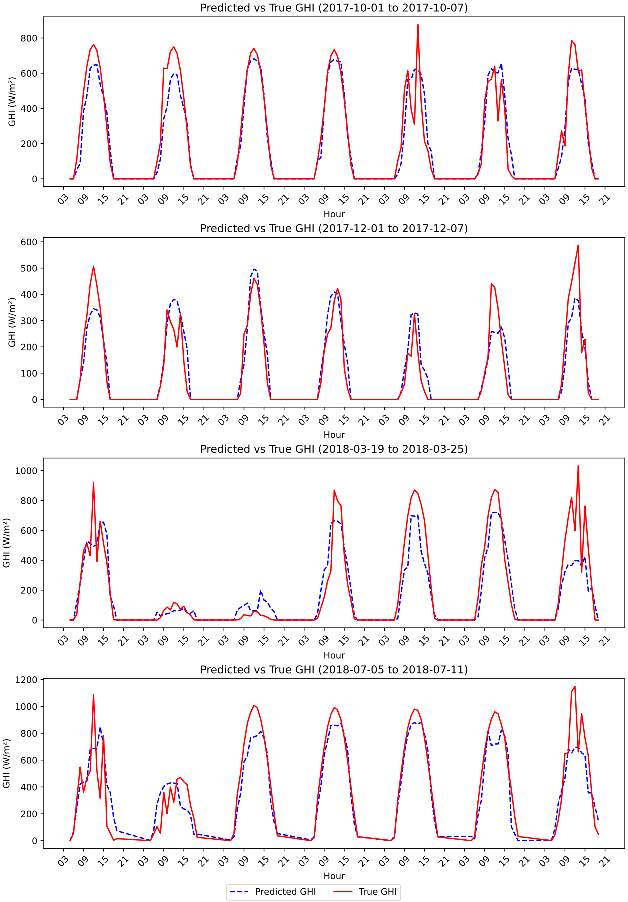

Figure 11. Predicted and true hourly GHI

Figure 13 shows the RMSE, MAE, and MBE metrics for this model using DNI and DHI inputs from three separation models.

Despite variations in GHI and DNI, RMSE and MAE remain consistent at approximately 220 W/m^2 and 160 W/m^2, respectively, with minimal POA discrepancies in MBE. Seasonality has little impact on RMSE and MAE, but MBE varies significantly. Winter and fall introduce a bias of about –50 W/m^2, nearly double that of summer and spring, making bias-free predictions more challenging.

The POA irradiance output serves as the input for the subsequent phase in the physical model chain, the reflection loss model and the cell temperature model.

4.2.3 Reflection Loss

A portion of POA irradiance is reflected back to the sky, which depends on the tilt angle of the surface and the incoming solar angle, resulting in effective irradiance

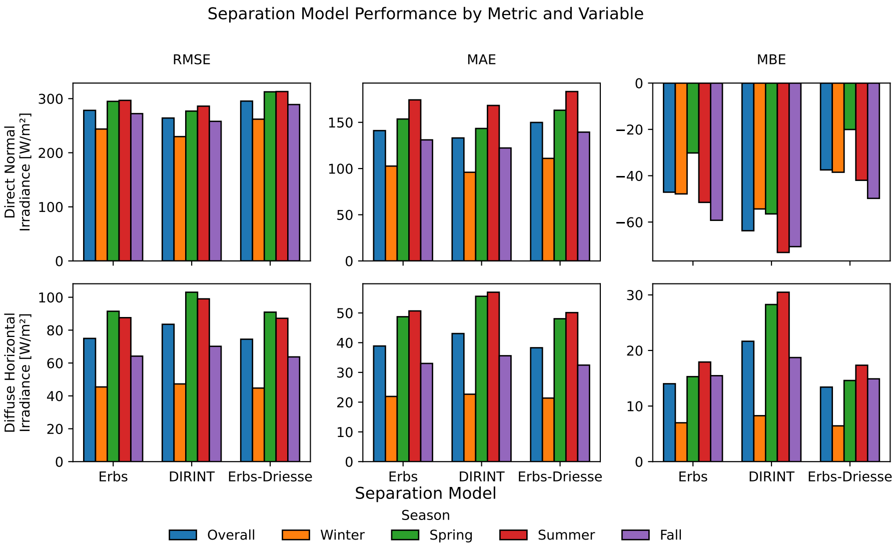

Figure 12. Separation model performance

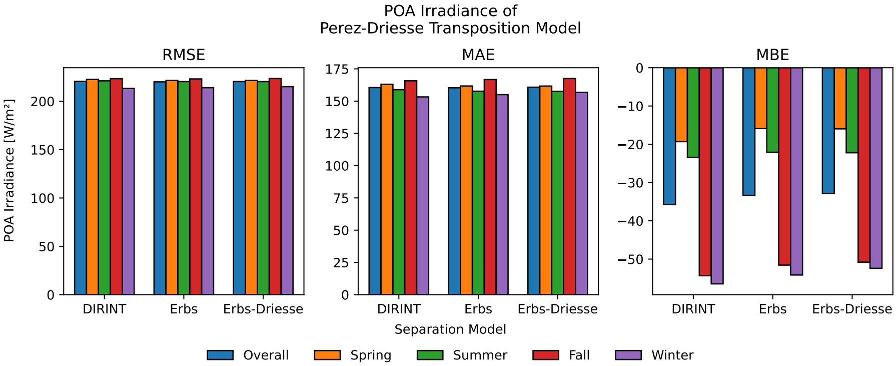

Figure 13. Transposition model performance

that is always lower than POA irradiance. Figure 14 shows daily and seasonal mean reflection losses from three models. The Martin-Ruiz model has the lowest overall loss (3.4%), while the Physical model, based on Fresnel's laws, reflects 3.9% of POA, peaking at 4.3% in winter. All models follow a similar seasonal pattern, with the highest losses in winter and lower losses in other seasons. The ASHRAE model performs slightly better than the Physical model, with a 3.6% overall loss.

Across all models, 3.4%–3.9% of POA is reflected, leaving 96% as effective irradiance, which is then passed to the PV model.

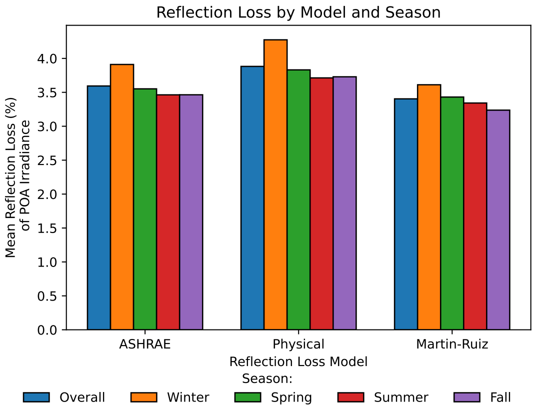

Figure 14. Average reflection losses of the POA irradiance

4.2.4 Cell Temperature

Cell temperature model is used to observe the operating temperature of PV cells based on POA irradiance, ambient temperature, wind speed, and the specific properties of the PV panel. The module-backsheet temperature and the ambient temperature data are used as the reference of the cell temperature. The temperature delta between those two references and the cell temperature model is as shown in Figure 15. The results indicate that for all tested models, the overall and seasonal temperature delta between the cell temperature and the module-backsheet temperature remains below 2°C, except during the summer, when the delta approaches 3°C. In terms of ambient

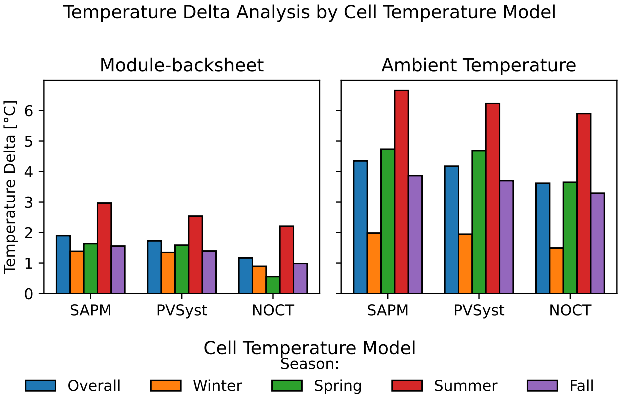

Figure 15. Average temperature delta

temperature, the temperature delta against the cell temperature is below 5°C for all models in every season except in the summer where the temperature delta reaches its highest value, up to 6.8°C.

4.2.5 PV Model

The PV model generates DC power output using cell temperature and effective irradiance from the reflection loss model. The Evans model provides only DC power, while the De Soto model outputs voltage, current, and power. Figure 16 displays their performance, showing nearly identical RMSE and MAE values in both magnitude and seasonal patterns. The overall RMSE is 38.8 kW, and the MAE is 19.7 kW. The key difference between the two models lies in MBE performance. The Evans model exhibits a lower bias at –5.21 kW, while the De Soto model has –9.15 kW, indicating both models underestimate power output, though Evans does so less. With a total PV capacity of 271 kW, the RMSE of 38.8 kW corresponds to an average prediction error of 14% of installed capacity, highlighting the forecast's uncertainty relative to the system's maximum potential.

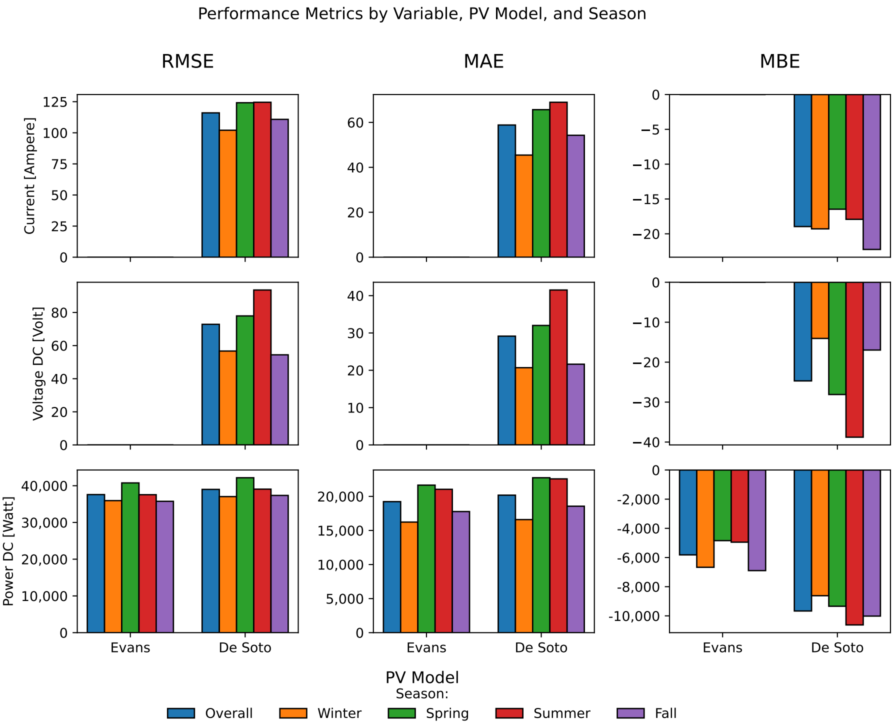

Figure 16. PV model performance

4.2.6 AC Power Forecast

The AC power forecast is the final output of this framework, derived from the PV model's DC power using inverter specifications. As shown in Table 9, 54 (3 × 1 × 3 × 3 × 2) physical model combinations were evaluated based on RMSE, MAE, and MBE. RMSE values range from 36.18 kW to 36.69 kW (13.35%–13.53% of the 271 kWp capacity), while MAE spans 18.38 kW to 19.07 kW (6.9%–7.03%). Given the minimal differences in RMSE and MAE, MBE serves as the primary ranking metric, emphasizing the influence of model selection on AC output.

Table 9 presents the top 10 model combinations, ranked by MBE, where values closer to zero indicate lower bias. The nMBE ranges from -2.03% to -0.29%. Further details are available in Section Appendix 1.

Table 9. Performance Comparison of Physical Model Chain Combinations

PV Model	Cell Temperature	Reflection Loss	Transposition	Separation	RMSE (kW)	MAE (kW)	MBE (kW)
Evans	NOCT	Martin-Ruiz	Perez-Driesse	Erbs-Driesse	36.42	18.51	-0.79
Evans	NOCT	Martin-Ruiz	Perez-Driesse	Erbs	36.38	18.46	-0.83
Evans	NOCT	ASHRAE	Perez-Driesse	Erbs-Driesse	36.51	18.64	-0.85
Evans	NOCT	ASHRAE	Perez-Driesse	Erbs	36.47	18.58	-0.91
Evans	NOCT	Physical	Perez-Driesse	Erbs-Driesse	36.37	18.47	-0.97
Evans	NOCT	Physical	Perez-Driesse	Erbs	36.33	18.42	-1.02
Evans	PVsyst	Martin-Ruiz	Perez-Driesse	Erbs-Driesse	36.31	18.50	-1.13
Evans	NOCT	Martin-Ruiz	Perez-Driesse	DIRINT	36.34	18.43	-1.15
Evans	NOCT	Martin-Ruiz	Perez-Driesse	Erbs	36.28	18.45	-1.17
Evans	PVsyst	ASHRAE	Perez-Driesse	Erbs-Driesse	36.41	18.63	-1.19

Table 9 confirms trends observed in Figure 12, where the Erbs and Erbs-Driesse models yield lower MBE values than DIRINT. Similarly, the Martin-Ruiz and ASHRAE models dominate the best-performing reflection loss models, aligning with Figure 14, which shows approximately 3.5% reflection loss for these models.

For cell temperature, the NOCT model outperforms others, consistent with Figure 15, where NOCT and PVsyst exhibit lower mean temperature deltas between cell and module-backsheet temperatures. Small temperature differences significantly impact AC power output. Additionally, the Evans PV model outperforms the more complex De Soto model, reaffirming Figure 16, where Evans consistently surpasses De Soto.

Overall, minimizing errors in each phase of the physical model chain improves AC power predictions. Notably, the separation and transposition models contribute the highest irradiance RMSE, making them critical for accurate irradiance estimation. Meanwhile, only about 3% of the irradiance is reflected, while 96% is absorbed and converted into electricity.

Table 10 compares the AC power output (kW) forecast performance of the proposed hybrid method, persistence forecast, and LSTM-based data-driven forecast across different training durations. Each model chain step is numerically encoded according to its order, as defined in Table 3. For the LSTM model, all NWP ENS and NWP HRES variables listed in Table 3 are used as predictors.

Table 10. Performance of the Proposed Method

Model	Model chain combination	RMSE	MAE	MBE
Proposed method (hybrid of XGBoost + physical model chain)	S3R3C3P1	36.42	18.51	**-0.79**
	S2R2C1P1	**36.18**	**18.39**	-1.79
	S3R1C1P2	36.67	**19.10**	-5.08
	S2R1C1P2	**36.70**	19.03	-5.41
	S2R2C1P2	36.55	18.89	**-5.52**
LSTM: Layer 1 (128 units, activation: tanh, dropout: 0.2) Layer 2 (128 units, activation: tanh, dropout: 0.2) Layer 3 (128 units, activation: ReLU, dropout: 0.2) Dense Layer	**Training Days**			
	3	42.18	30.04	-4.30
	7	38.55	25.96	-4.81
	14	71.61	51.52	19.87
	30	64.71	47.49	-12.56
	60	37.43	25.24	-1.59
	90	**36.04**	**23.31**	**-2.11**
	120	52.51	39.52	-9.62
	150	**36.14**	**24.93**	**-2.36**
	180	**34.14**	**22.98**	**-1.23**
	360	50.18	35.68	-14.07
Persistence	NA	**47.40**	**22.36**	**-0.13**

The results confirm that the proposed hybrid method outperforms the persistence forecast in both RMSE and MAE. When the LSTM model is trained on fewer than 60 days of historical data, its RMSE exceeds that of the proposed method. However, the best-performing LSTM models (trained on 90, 150, and 180 days) achieve a slightly lower MAE than the proposed approach.

Figure 17 provides the sample of the predicted AC power, true AC power, and actual GHI at a 15-minute temporal resolution for the same first two weeks as the hourly predicted GHI shown in Figure 11. The predicted AC power values correspond to those produced by the best-performing model chain, S3R3C3P1, listed in Table 9, which has an MBE of -0.79 kW.

The true output power generally follows the pattern of the actual GHI. However, on days with highly fluctuating irradiance, such as October 5, 2017, the forecasted power is less accurate compared to days with more stable irradiance, such as December 4, 2017.

5. Conclusion and Future Work

This study investigated day-ahead PV power forecasting using ECMWF NWP data. ECMWF ENS data was utilized for hourly GHI prediction, while ECMWF HRES data supported the physical model chain calculation. Unlike the deep learning method such as LSTM, the proposed method requires minimal historical data, enables immediate PV power forecasting following PV plant commissioning. Thus, it offers a viable alternative where long historical datasets are unavailable. By applying periodic retraining mechanism the model effectively adapts to changing conditions, enhancing forecasting accuracy. The physical model chain improves understanding of how PV system components interact to convert solar irradiation into AC power.

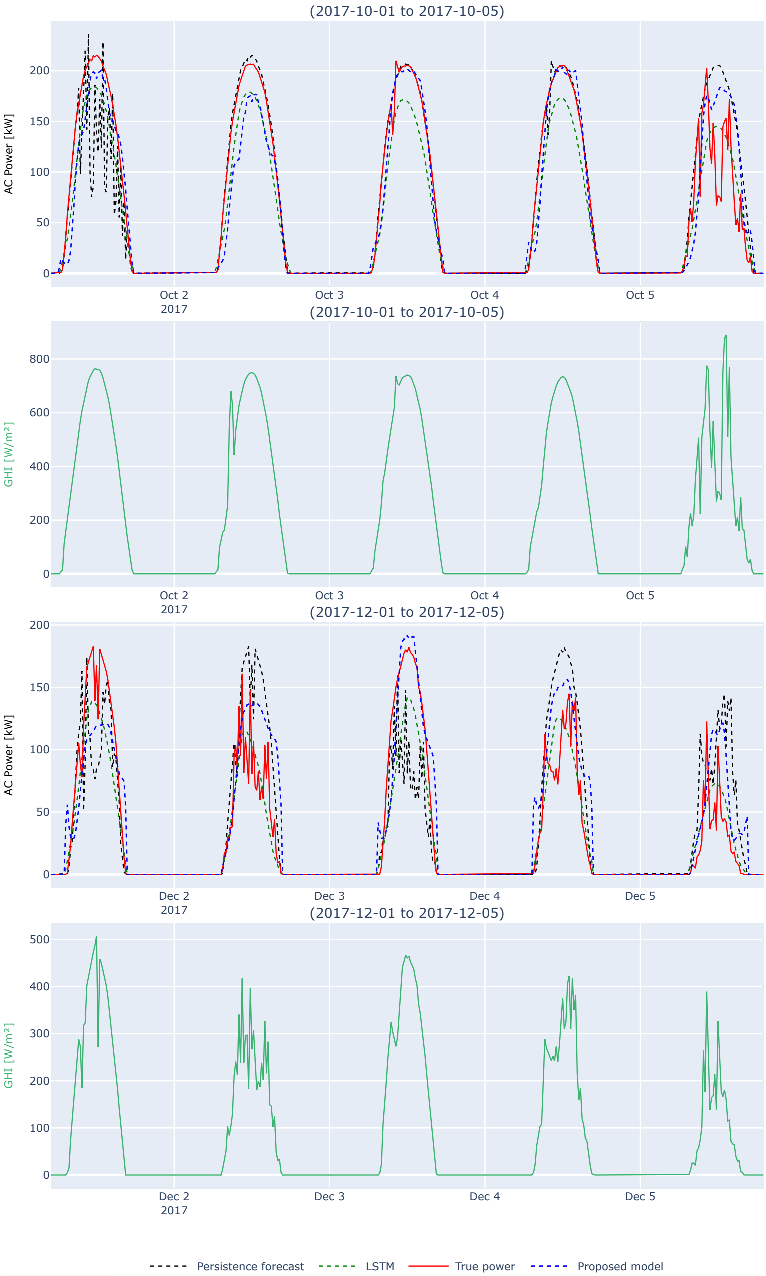

Figure 17. Predicted 15-min PV AC power output-1

Day-ahead NWP data tends to underestimate actual GHI, primarily due to challenges in capturing rapid cloud dynamics and motion, leading to discrepancies between predicted and actual irradiance levels. Further advancements may involve integrating additional data sources, such as satellite imagery to improve predictions under rapidly changing atmospheric conditions.

Acknowledgement

The authors would like to acknowledge the National Taiwan University of Science and Technology (NTUST) and Universitas Indonesia (UI) for their academic support.

Funding Statement I would like to thank PT. Perusahaan Listrik Negara-PLN Persero) for granting the scholarship and supporting this research.

Competing Interests The authors declare that they have no competing financial interests or personal relationships that could have influenced the work reported in this paper.

References

[1] David Feldman et al. *US solar photovoltaic system and energy storage cost benchmark (Q1 2020)*. Tech. rep. National Renewable Energy Lab.(NREL), Golden, CO (United States), 2021.

[2] Felix Creutzig et al. "Technological innovation enables low cost climate change mitigation". In: *Energy Research & Social Science* 105 (2023), p. 103276.

[3] Dolf Gielen et al. "The role of renewable energy in the global energy transformation". In: *Energy Strategy Reviews* 24 (2019), pp. 38–50.

[4] Dazhi Yang et al. "A review of solar forecasting, its dependence on atmospheric sciences and implications for grid integration: Towards carbon neutrality". In: *Renewable and Sustainable Energy Reviews* 161 (2022), p. 112348.

[5] Martin János Mayer. "Benefits of physical and machine learning hybridization for photovoltaic power forecasting". In: *Renewable and Sustainable Energy Reviews* 168 (2022), p. 112772.

[6] Hugo TC Pedro et al. "Assessment of machine learning techniques for deterministic and probabilistic intra-hour solar forecasts". In: *Renewable Energy* 123 (2018), pp. 191–203.

[7] Lennard Visser, Tarek AlSkaif, and Wilfried van Sark. "Operational day-ahead solar power forecasting for aggregated PV systems with a varying spatial distribution". In: *Renewable Energy* 183 (2022), pp. 267–282.

[8] Kejun Wang, Xiaoxia Qi, and Hongda Liu. "A comparison of day-ahead photovoltaic power forecasting models based on deep learning neural network". In: *Applied Energy* 251 (2019), p. 113315.

[9] Wenting Wang et al. "An archived dataset from the ECMWF Ensemble Prediction System for probabilistic solar power forecasting". In: *Solar Energy* 248 (2022), pp. 64–75.

[10] Dazhi Yang, Wenting Wang, and Tao Hong. "A historical weather forecast dataset from the European Centre for Medium-Range Weather Forecasts (ECMWF) for energy forecasting". In: *Solar Energy* 232 (Jan. 2022), pp. 263–274. ISSN: 0038092X. DOI: 10.1016/j.solener.2021.12.011.

[11] Christina Brester et al. "Evaluating neural network models in site-specific solar PV forecasting using numerical weather prediction data and weather observations". In: *Renewable Energy* 207 (2023), pp. 266–274.

[12] Alejandro Catalina, Carlos M. Alaiz, and Jose R. Dorronsoro. "Combining numerical weather predictions and satellite data for PV energy nowcasting". In: *IEEE Transactions on Sustainable Energy* 11.3 (July 2020), pp. 1930–1937. ISSN: 1949-3029. DOI: 10.1109/TSTE.2019.2946621.

[13] Martin János Mayer and Gyula Gróf. "Extensive comparison of physical models for photovoltaic power forecasting". In: *Applied Energy* 283 (2021), p. 116239.

[14] Dazhi Yang. “Standard of reference in operational day-ahead deterministic solar forecasting”. In: *Journal of Renewable and Sustainable Energy* 11.5 (Sept. 2019), p. 053702. ISSN: 1941-7012. DOI: 10.1063/1.5114985. eprint: https://pubs.aip.org/aip/jrse/article-pdf/doi/10.1063/1.5114985/14016237/053702_1_online.pdf. URL: https://doi.org/10.1063/1.5114985.

[15] Yuri V. Makarov et al. “Incorporating Uncertainty of Wind Power Generation Forecast Into Power System Operation, Dispatch, and Unit Commitment Procedures”. In: *IEEE Transactions on Sustainable Energy* 2.4 (2011), pp. 433–442. DOI: 10.1109/TSTE.2011.2159254.

[16] Dazhi Yang et al. “Operational solar forecasting for grid integration: Standards, challenges, and outlook”. In: *Solar Energy* 224 (2021), pp. 930–937.

[17] Martin János Mayer and Dazhi Yang. “Pairing ensemble numerical weather prediction with ensemble physical model chain for probabilistic photovoltaic power forecasting”. In: *Renewable and Sustainable Energy Reviews* 175 (2023), p. 113171.

[18] Rui Guo et al. “Degradation state recognition of piston pump based on ICEEMDAN and XGBoost”. In: *Applied Sciences* 10.18 (2020), p. 6593.

[19] DG Erbs, SA Klein, and JA Duffie. “Estimation of the diffuse radiation fraction for hourly, daily and monthly-average global radiation”. In: *Solar Energy* 28.4 (1982), pp. 293–302.

[20] Richard Perez et al. “Modeling daylight availability and irradiance components from direct and global irradiance”. In: *Solar Energy* 44.5 (1990), pp. 271–289.

[21] Anton Driesse, Adam R Jensen, and Richard Perez. “A continuous form of the Perez diffuse sky model for forward and reverse transposition”. In: *Solar Energy* 267 (Jan. 2024), p. 112093.

[22] AF Souka and HH Safwat. “Determination of the optimum orientations for the double-exposure, flat-plate collector and its reflectors”. In: *Solar Energy* 10.4 (1966), pp. 170–174.

[23] Widalys De Soto, Sanford A Klein, and William A Beckman. “Improvement and validation of a model for photovoltaic array performance”. In: *Solar Energy* 80.1 (2006), pp. 78–88.

[24] N Martin and JM Ruiz. “Corrigendum to “Calculation of the PV modules angular losses under field conditions by means of an analytical model” [Solar Energy Materials and Solar Cells 70 (1) (2001) 25–38]”. In: *Solar Energy Materials and Solar Cells* 110 (2013), p. 154.

[25] Jay A Kratochvil, William Earl Boyson, and David L King. *Photovoltaic array performance model*. Tech. rep. Sandia National Laboratories (SNL), Albuquerque, NM, and Livermore, CA, 2004.

[26] David Faiman. “Assessing the outdoor operating temperature of photovoltaic modules”. In: *Progress in Photovoltaics: Research and Applications* 16.4 (2008), pp. 307–315.

[27] Paul Gilman et al. “SAM photovoltaic model technical reference update”. In: *NREL: Golden, CO, USA* (2018).

[28] Aron P Dobos. *PVWatts version 5 manual*. Tech. rep. National Renewable Energy Lab.(NREL), Golden, CO (United States), 2014.

[29] DL Evans. “Simplified method for predicting photovoltaic array output”. In: *Solar Energy* 27.6 (1981), pp. 555–560.

[30] Matthew T Boyd. “High-speed monitoring of multiple grid-connected photovoltaic array configurations and supplementary weather station”. In: *Journal of Solar Energy Engineering* 139.3 (2017), p. 034502.

[31] Matthew Boyd. *NIST Weather Station for Photovoltaic and Building System Research*. Technical Note 1913. Gaithersburg, MD: National Institute of Standards and Technology, 2016.

Appendix 1. Appendix

Table 11. Performance Comparison of Physical Model Chain Combinations

PV Model	Cell Temp.	Reflection Loss	Transposition	Separation	RMSE (kW)	MAE (kW)	MBE (kW)
Evans	NOCT	Martin-Ruiz	Perez-Driesse	Erbs-Driesse	36.42	18.51	-0.79
Evans	NOCT	Martin-Ruiz	Perez-Driesse	Erbs	36.38	18.46	-0.83
Evans	NOCT	ASHRAE	Perez-Driesse	Erbs-Driesse	36.51	18.64	-0.85
Evans	NOCT	ASHRAE	Perez-Driesse	Erbs	36.47	18.58	-0.91
Evans	NOCT	Physical	Perez-Driesse	Erbs-Driesse	36.37	18.47	-0.97
Evans	NOCT	Physical	Perez-Driesse	Erbs	36.33	18.42	-1.02
Evans	PVSyst	Martin-Ruiz	Perez-Driesse	Erbs-Driesse	36.31	18.50	-1.13
Evans	NOCT	Martin-Ruiz	Perez-Driesse	DIRINT	36.34	18.43	-1.15
Evans	PVSyst	Martin-Ruiz	Perez-Driesse	Erbs	36.28	18.45	-1.17
Evans	PVSyst	ASHRAE	Perez-Driesse	Erbs-Driesse	36.41	18.63	-1.19
Evans	NOCT	ASHRAE	Perez-Driesse	DIRINT	36.42	18.55	-1.23
Evans	SAPM	Martin-Ruiz	Perez-Driesse	Erbs-Driesse	36.29	18.51	-1.24
Evans	PVSyst	ASHRAE	Perez-Driesse	Erbs	36.37	18.57	-1.25
Evans	SAPM	Martin-Ruiz	Perez-Driesse	Erbs	36.25	18.46	-1.29
Evans	SAPM	ASHRAE	Perez-Driesse	Erbs-Driesse	36.39	18.63	-1.31
Evans	PVSyst	Physical	Perez-Driesse	Erbs-Driesse	36.26	18.45	-1.31
Evans	NOCT	Physical	Perez-Driesse	DIRINT	36.30	18.39	-1.34
Evans	PVSyst	Physical	Perez-Driesse	Erbs	36.23	18.41	-1.36
Evans	SAPM	ASHRAE	Perez-Driesse	Erbs	36.34	18.58	-1.36
Evans	SAPM	Physical	Perez-Driesse	Erbs-Driesse	36.24	18.46	-1.43
Evans	SAPM	Physical	Perez-Driesse	Erbs	36.20	18.42	-1.48
Evans	PVSyst	Martin-Ruiz	Perez-Driesse	DIRINT	36.25	18.42	-1.49
Evans	PVSyst	ASHRAE	Perez-Driesse	DIRINT	36.33	18.54	-1.56
Evans	SAPM	Martin-Ruiz	Perez-Driesse	DIRINT	36.22	18.43	-1.60
Evans	PVSyst	Physical	Perez-Driesse	DIRINT	36.21	18.38	-1.67
Evans	SAPM	ASHRAE	Perez-Driesse	DIRINT	36.31	18.55	-1.68
Evans	SAPM	Physical	Perez-Driesse	DIRINT	36.18	18.39	-1.79
De Soto	NOCT	Martin-Ruiz	Perez-Driesse	Erbs-Driesse	36.47	18.88	-4.55
De Soto	NOCT	Martin-Ruiz	Perez-Driesse	Erbs	36.44	18.84	-4.59
De Soto	NOCT	ASHRAE	Perez-Driesse	Erbs-Driesse	36.61	19.01	-4.60
De Soto	NOCT	ASHRAE	Perez-Driesse	Erbs	36.57	18.96	-4.65
De Soto	NOCT	Physical	Perez-Driesse	Erbs-Driesse	36.45	18.86	-4.72
De Soto	NOCT	Physical	Perez-Driesse	Erbs	36.42	18.81	-4.76
De Soto	PVSyst	Martin-Ruiz	Perez-Driesse	Erbs-Driesse	36.50	18.93	-4.91
De Soto	PVSyst	ASHRAE	Perez-Driesse	Erbs-Driesse	36.64	19.06	-4.96
De Soto	PVSyst	ASHRAE	Perez-Driesse	Erbs	36.60	19.01	-5.01
De Soto	SAPM	Martin-Ruiz	Perez-Driesse	Erbs-Driesse	36.53	18.97	-5.03
De Soto	NOCT	Physical	Perez-Driesse	DIRINT	36.48	18.79	-5.04
De Soto	SAPM	Martin-Ruiz	Perez-Driesse	Erbs	36.50	18.92	-5.08
De Soto	PVSyst	Physical	Perez-Driesse	Erbs-Driesse	36.48	18.91	-5.08
De Soto	SAPM	ASHRAE	Perez-Driesse	Erbs-Driesse	36.67	19.10	-5.08
De Soto	PVSyst	Physical	Perez-Driesse	Erbs	36.45	18.86	-5.12
De Soto	SAPM	ASHRAE	Perez-Driesse	Erbs	36.64	19.05	-5.13
De Soto	SAPM	Physical	Perez-Driesse	Erbs-Driesse	36.51	18.95	-5.20
De Soto	PVSyst	Martin-Ruiz	Perez-Driesse	DIRINT	36.54	18.87	-5.22
De Soto	SAPM	Physical	Perez-Driesse	Erbs	36.48	18.90	-5.25
De Soto	PVSyst	ASHRAE	Perez-Driesse	DIRINT	36.66	18.99	-5.29
De Soto	SAPM	Martin-Ruiz	Perez-Driesse	DIRINT	36.57	18.91	-5.35

Continued on next page

PV Model	Cell Temp.	Reflection Loss	Transposition	Separation	RMSE (kW)	MAE (kW)	MBE (kW)
De Soto	PVSyst	Physical	Perez-Driesse	DIRINT	36.52	18.85	-5.39
De Soto	SAPM	ASHRAE	Perez-Driesse	DIRINT	36.70	19.03	-5.41
De Soto	SAPM	Physical	Perez-Driesse	DIRINT	36.55	18.89	-5.52